Research Article

Kinematic modeling and stability analysis for a wind turbine blade inspection robot

Jindan WANG[1], Xiaolong MA[1], Xinghan ZHU[1], Xin WANG[2], Lan ZHANG[2], Binrui WANG[1 ✉]

[1]*College of Mechanical and Electrical Engineering, China Jiliang University, Hangzhou 310018, China*
[2]*Zhejiang Lab, Hangzhou 311121, China*

Abstract: Robots are used to conduct non-destructive defect detection on wind turbine blades and monitor their integrity over time. However, current inspection robots are often bulky, heavy, and struggle to detect defects in the blade's main beam, thus presenting difficulties in portability and effectiveness. To address these issues, we design a wheel-wing composite robot equipped with a curved surface-adaptive phased array ultrasonic detection device for the detection of defects in the wind turbine blade's main beam. We determine the pose equation under different section characteristics and identify the robot's stable range of motion, thus developing a model of its kinematics. A detection device adapted for variable curvature surfaces is designed to ensure tight coupling between the robot's probe and the blade. Additionally, element differential and least squares ellipse-fitting methods are employed to analyze blades with irregular sections. The simulation results demonstrate that the prototype can stably traverse an area with a vertical angle of $\pm14.06°$ at a speed of 0.25 m/s, fully covering the main beam area of the blade during walking operations. Moreover, the robot can scan the main beam area at a speed of 0.1 m/s, enabling the accurate detection of defects.

Key words: Composite robot; Wind turbine blades; Surface of variable curvature; Stability; Nondestructive testing

1 Introduction

Wind turbine blades (WTB) are exposed to outdoor conditions for extended periods, making them susceptible to issues such as blade cracking, lightning strike damage, main beam fractures, and other problems. Left undetected, the gradual accumulation of microdamage can result in significant harm, and impact the efficiency of wind power generation. Severe damage can lead to wind turbine shutdown or even collapse, with potentially catastrophic consequences (Chou et al., 2019). Given that the main beam serves as the primary support structure of the blade (Civera et al., 2022), regular detection of flaws within this structure is essential to prevent minor damage from escalating. However,

many flaws are challenging to detect at an early stage using conventional methods. Robotic systems are increasingly being used for damage detection, but they can still struggle to achieve accurate results, and they have bulky designs. Therefore, our main objective is to develop a lightweight robot for WTB flaw detection, which can improve the inspection of WTB main beams.

In recent years, a diverse range of wind turbine inspection robots has been developed. Examples include the fan blade duct endoscope tracking robot (Zhang et al., 2021), the fan maintenance multi-robot system (Franko et al., 2020), the detection drone (Wang et al., 2023), and the fan climbing robot (Padrigalan and Liu, 2023). These robots can be broadly categorized into contact detection robots and non-contact detection robots.

Non-contact detection primarily relies on UAV-based visual inspection methods. For instance, Car et al. (2020) developed a strategy for wind turbine blade detection utilizing a UAV equipped with Li-DAR technology. Going further, Jung et al. (2015) introduced a micro-aerial wall-climbing robot capable of gliding, adhering, and maneuvering on both verti-

✉ Binrui WANG, wangbrpaper@163.com

🔟 Jindan WANG, https://orcid.org/0009-0001-9711-7488
Binrui WANG, https://orcid.org/0000-0002-8955-4055

cal and non-sliding surfaces. Additionally, Gu et al. (2019) proposed a comprehensive design for autonomous wind turbine inspection using a quadrotor aircraft outfitted with high-resolution cameras and 2D LiDAR, and performed tests to demonstrate the success of the design. As a final example, Kocer et al. (2018) developed an aerial robot that can ascend to high altitudes for wind turbine maintenance, and introduced a novel aerial robotic arm design that integrates online detection and decision-making to address wind turbine maintenance challenges. However, a common limitation of these visual-based inspection approaches is that they can be negatively impacted by environmental factors.

Contact detection robots can be further categorized based on different contact modes. One such method involves vacuum adsorption between the suction cup and the blade, while another method utilizes ropes or mechanical mechanisms for magnetic adsorption to secure the equipment. For instance, Blade BUG, a robotics company based in London, has developed a six-legged crawling robot for WTB inspection that utilizes a vacuum adsorption structure to ensure operational stability. The study by Cieslak et al. (2023) specifically introduces the design, testing, and in-service operation of this hexapod robot, as well as the selection of conditions for its deployment. They conducted walking tests and functional demonstrations of the robot, verifying the feasibility of its use. The Danish company Rope Robotics has created a robot for WTB inspection capable of both repair and inspection, although it requires multiple ropes to control the movement of the body on the blade (Sabel and Abbas, 2019). Additionally, Hayashi et al. (2017) proposed a robot that can use blades as a guide for vertical motion, though again this necessitated multiple ropes and cables to guide the robot. As another example, Lee et al. (2016) designed a novel robotic system for the operation and maintenance (O&M) of 5 MW offshore wind turbines. This system involves a mobile platform utilizing a linear drive parallel mechanism for vertical climbing on the turbine tower and blade. The manipulator is equipped with a phased array ultrasonic testing (PAUT) device for cleaning and inspection. Experimental tests demonstrated that this proposed robotic system and control scheme can resist disturbances from wind, thus enabling wind turbine operation and maintenance tasks during in-spection. Sadeghian and Sareh (2021) have also made significant contributions to research on WTB inspection robots. First, they designed a mechanical arm for WTB maintenance, capable of tasks such as cleaning, polishing, defect filling, and general maintenance. An exceptional feature of this mechanical arm is its ability to replace the end effector as needed, to mimic the user's hand movements, and to provide sensory feedback. Furthermore, in order to enhance the application of the robotic arm in the operation and maintenance of WTBs, they developed a robotic system specifically for wind turbine airfoil maintenance. The robot's rover can move along the blade while the machinery mounted above it can carry out simple operational and maintenance tasks (Sahni et al., 2022). Additionally, Sareh and Sadeghian (2022) designed a hexapod adsorption robot, integrating their designed robot arm to enhance blade maintenance capabilities. This integration allows for more efficient completion of blade maintenance tasks.

The contact detection method addresses the challenge of securing the structural integrity, although it leads to another issue of the coupling contact between the detection mechanism and the target area. To address the challenge of adapting to surface changes (such as variable curvature) in detection equipment, a wall-climbing robot operating system based on a permanent magnet wheel wall-climbing robot was proposed (Xu et al., 2022). This system is equipped with operation execution modules for cleaning, detection, and maintenance. The robot's phased array ultrasonic detection module is closely fitted to the detection surface through a connecting rod bracket structure and magnetic adsorption module. Li et al. (2019) also designed a wall-climbing robot with an integrated ultrasonic detection system. This system features a double-joint design, with the rotary compression joint being driven by a steering machine to allow adhesion to the wall and automatic adaptation to uneven surfaces. These innovative methods showcase the potential for adaptive adhesion to uncertain contact surfaces by modifying the mechanical structure. In a similar vein, Guo et al. (2017) conducted a comprehensive study on a curved bipedal wall-climbing robot designed for wind power blade detection. They analyzed the robot's force posture on the blade surface and explored flexibility control and adaptive adsorption of the contact force. Continuing

this trend, Wang et al. (2021) developed a flexible wall-climbing robot with an adaptive variable curvature facade, and analyzed the robot's attitude changes and adaptive motion characteristics on the tower barrel surface. Looking further into the kinematics of such devices, Song et al. (2016) conducted pose description and established a kinematic model for a barrel-wheeled mobile inspection robot. Additionally, Joshua et al. (2016) established the kinematic model of a robot on irregular surfaces, proposed motion control methods for mobile robots on surfaces, and offered insights into maximizing the stability of robots on surfaces. Similar examples can be found in marine applications as well, for instance Fan et al. (2018) investigated the adsorption and sliding stability of underwater pipeline inspection robots under buoyancy and wave forces. Collectively, these studies advanced the development of adaptive and stable robotic systems for WTB flaw detection.

Existing research on inspection robots highlights several challenges that need to be addressed to achieve more effective results. These challenges include reducing the volume and weight of the detection robot, achieving convenient high-altitude deployment, improving detection efficiency, and utilizing a simple mechanism design that enables adaptive attitude adjustment of the detection equipment and stability of the robot's motion on the surface.

To address these challenges and optimize the overall structure of the detection robot, we propose a wheel-wing composite robot equipped with surface adaptive detection equipment to inspect the main beam blade. By integrating a UAV with a wheeled mobile robot, the weight and volume of the detection robot body can be minimized, allowing for easy and rapid deployment to the desired position of the blade for high-altitude detection. A passive adaptive detection mechanism is designed for wind power blade surfaces with variable curvature, facilitating the adaptive coupling of the detection equipment. Furthermore, the design of a variable wheelbase wheel chassis can enhance the application range and detection efficiency of the robot. We validate the effectiveness of the robot's structural design through prototype testing and simulations.

2 Robot design scheme

The structural design of the wheel-wing composite robot, as illustrated in Fig. 1, is comprised of a four-rotor UAV, the detection vehicle body, the surface adaptive phased array ultrasonic detection mechanism, and the electrical control equipment. The UAV is a high-load, high-power four-rotor model capable of carrying a 15 kg load and taking off at a relative height of less than 200 m, enabling remote transportation to the top of high-altitude blades. The detection vehicle body is constructed using 2020 high-strength aluminum profiles to ensure robustness, featuring a four-wheel differential design with two high-load, high-power hub motors serving as the rear driving wheels. There is an encoder in the wheel motor that can be utilized to ascertain the position of the robot during movement. These motors allow for robot attitude adjustment through differential speed, while the front wheel acts as a fixed rubber support to maintain stability. The dimensions of the vehicle body are tailored to the common blade curvature, enabling adaptation to the outer surfaces of most WTB. To enhance versatility, the front and rear wheel connection plates are designed with adjustable spacing, allowing for customization based on specific requirements. Additionally, a passive adaptive detection mechanism is designed to facilitate the adaptive coupling of the detection equipment to variable curvature surfaces, ensuring precision of detection. The prototype is shown in Fig. 2.
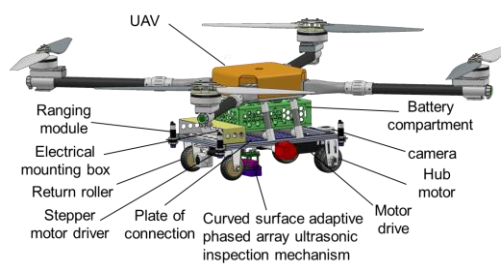

Fig. 1 Structural diagram of the wheel-wing composite robot

Fig. 2 Photo of the wheel-wing composite robot

Due to the variable curvature surface of the main blade, a rigid connection cannot guarantee full adhesive contact between the probe and the blade surface, as the probe needs to maintain full contact with the contact surface throughout operations. To address this issue, a self-adapting method has been designed. As shown in Fig. 3, the scanning mechanism of the surface consists of a sliding block connected to a long connecting screw via a connecting plate, a floating joint connected to the long connecting screw, and a short connecting screw connected beneath the floating joint. This setup allows the probe to move at an optimal angle in the scanning direction, thereby achieving vertical contact between the probe and the contact surface. The floating joint is connected to the lower guide plate via the short connection screw, and the guide plate's four corners are fitted with mounting holes. The guide rod, equipped with a spring, is connected to the probe assembly via a water pipe connection block. The guide plate can transfer the upper and lower components of the force to the spring, and therefore scanning at different positions will apply different pressures between the probe and the contact surface. Under the joint action of the floating joint and the spring, tight coupling between the probe and the contact surface can be achieved, reducing the consumption of the coupling agent and ensuring high detection accuracy. The ultrasonic detection probe model number is 1L64-1.5x22-MW5-F2.5-D3, the shell size is L112xW35xH50m, the center frequency is 1 MHz, the number of array elements is 64, and the probe element is linear scanning with 0°, which can cover a distance of 30 mm to 90 mm. It can detect internal defects of glass fiber-reinforced plastic laminate structures, which meets our testing requirements. The probe is shown in Fig. 4.
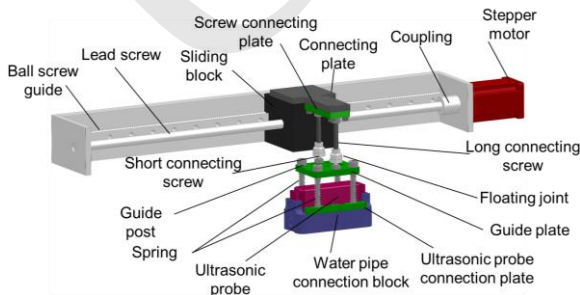
Fig. 3 Surface adaptive scanner composition

Fig. 4 Phased array ultrasonic probe

The operation of the wheel-wing composite robot is depicted in Fig. 5, which involves six main steps: (A) initial take-off; (B) hovering; (C) landing; (D) performing testing tasks; (E) take-off from the blade; (F) return; and (G) landing at the designated position.


Fig. 5 Composite robot operation diagram

3 Robot pose analysis

To facilitate analysis of the robot's motion, we assume that the wheel and surface make contact at a single point, and that the wheel is a rigid disk with no deformation. Furthermore, within the stable operating range of the robot on the curved surface, the relative motion between the wheel and contact surface is considered to be purely rolling. Since the root of the blade is approximately cylindrical in shape, a curved surface has been selected for this study.

3.1 Single wheel surface pure rolling motion

As depicted in Fig. 6, The origin of the absolute coordinate system is located at the center of one end of the cylinder, The X-axis aligns with the central axis of the cylinder, while the Z-axis corresponds to the opposite direction of gravity. Lastly, the Y-axis is determined by using the right-hand rule to establish a

single wheel's absolute coordinate system on the cylinder. The tangent plane of the cylinder and the tangent line m to the circle of the wheel intersect at the point t_1. The angle between the normal vectors t_1t_2 and t_1O of the tangent plane is ϑ, and the angle between m and the bus bar l of the cylinder is α. As shown in Fig. 6, a moving coordinate system is established with the tangent vector ε, principal normal λ and vice normal κ at the contact point t_1 of the curve as coordinate axes.
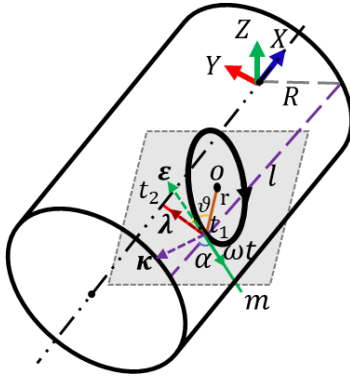
Fig. 6 Single wheel absolute coordinate system and Moving coordinate system

When the wheel is rolling purely on the cylinder at an angular velocity ω, the set of contact points on the cylinder with the wheel is:

$$\begin{cases} x = -\omega tr \cos(\alpha) \\ y = R\cos(\dfrac{-\omega tr \cos(\alpha)}{R}), \\ z = R\sin(\dfrac{-\omega tr \cos(\alpha)}{R}) \end{cases} \quad (1)$$

The matrix can be expressed as:

$$\boldsymbol{O} = \begin{bmatrix} -\omega tr \cos\alpha \\ R\cos(\dfrac{-\omega tr \cos\alpha}{R}) \\ R\sin(\dfrac{-\omega tr \cos\alpha}{R}) \end{bmatrix}, \quad (2)$$

The coordinate of the wheel center in the moving coordinate system is $(0, r\cos\vartheta, r\sin\vartheta)$, here $\boldsymbol{D}$ is the transition matrix, which is expressed in the absolute

coordinate system as:

$$\begin{bmatrix} x \\ y \\ z \\ 1 \end{bmatrix} = \boldsymbol{D} \begin{bmatrix} 0 \\ r\cos\vartheta \\ r\sin\vartheta \\ 1 \end{bmatrix}, \quad (3)$$

By using the wheel center's position in the absolute coordinate system, the velocity of the wheel center can be obtained as:

$$\|\boldsymbol{v}\| = \sqrt{\dot{x}^2 + \dot{y}^2 + \dot{z}^2}. \quad (4)$$

3.2 Pure rolling motion of the robot on the surface

The pose description of the robot can be expressed in terms of the absolute coordinates of a point on the robot (x, y, z) and the Euler angle (φ, θ, ψ). The rotation process is as follows: the robot first rotates φ about the x-axis, then rotates θ about the y-axis, and finally rotates ψ about the z-axis. For brevity in formula representation, the s is used to represent sin and the c is used to represent cos. The rotation matrix is as follows:

$$\boldsymbol{R} = \begin{bmatrix} c\varphi c\theta & c\varphi s\theta c\psi - s\varphi c\psi & c\varphi s\theta c\psi + s\varphi c\psi & 0 \\ s\varphi c\theta & s\varphi s\theta c\psi - c\varphi c\psi & s\varphi s\theta c\psi - c\varphi c\psi & 0 \\ -s\theta & c\theta s\psi & c\theta c\psi & 0 \\ 0 & 0 & 0 & 1 \end{bmatrix}, \quad (5)$$

$$\boldsymbol{D}^{(ij)} = \begin{bmatrix} \boldsymbol{R}(\psi & \theta & \varphi) & \boldsymbol{d}_{ij} \\ 0 & & 1 \end{bmatrix}, \quad (6)$$

$$\boldsymbol{d}_{ij} = \begin{bmatrix} x_0 & y_0 & z_0 \end{bmatrix}, \quad (7)$$

The coordinate system is established as shown in Fig. 7. The center point of the rear wheel axis H is taken as the origin of the moving coordinate system, the rear wheel axis HC is the positive direction of the y-axis, the line between the rear wheel axis and the front wheel axis is taken as the x-axis, and the vertical direction through the origin H and the XOY plane is taken as the z-axis. As shown in Fig. 7, A, B, C, D, and M are the centers of the wheels. The distance between the two rear wheels is b, and the distance between the
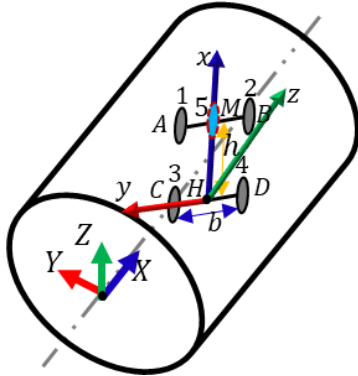
front and rear wheels is h.

Fig. 7 Coordinate system for the robot

The origin of the moving coordinate system in terms of the absolute coordinate system is (x_0, y_0, z_0). The coordinates of the robot's previous point are (x_1, y_1, z_1) in the moving coordinate system and (x, y, z) in the absolute coordinate system.

$$\begin{bmatrix} x \\ y \\ z \\ 1 \end{bmatrix} = \boldsymbol{D}^{(ij)} \begin{bmatrix} x_1 \\ y_1 \\ z_1 \\ 1 \end{bmatrix}. \tag{8}$$

The four wheels' center positions (C_A, C_B, C_C, C_D) in the moving coordinate system are $(h, b/2, 0)$, $(h, -b/2, 0)$, $(0, b/2, 0)$, $(0, -b/2, 0)$, respectively. Due to the limitations of the operating environment, the support wheel mainly plays a supporting role, which can be regarded as a wheel for analysis, and the two front wheels can be regarded as a single wheel, and the wheel center coordinate M is the center point of the axis of the two wheels $(h, 0, 0)$. The coordinates of the robot's three wheels in the global coordinate system can be obtained from the above formula.

$$\begin{bmatrix} x_M \\ y_M \\ z_M \\ 1 \end{bmatrix} = \begin{bmatrix} h(c\varphi c\psi + s\varphi s\theta s\psi) + x_0 \\ hc\theta s\psi + y_0 \\ h(-s\varphi c\psi + c\varphi s\theta s\psi) + z_0 \\ 1 \end{bmatrix}, \tag{9}$$

$$\begin{bmatrix} x_C \\ y_C \\ z_C \\ 1 \end{bmatrix} = \begin{bmatrix} \dfrac{b}{2}(-c\varphi s\psi + s\varphi s\theta c\psi) + x_0 \\ \dfrac{b}{2}c\theta c\psi + y_0 \\ \dfrac{b}{2}(s\varphi s\psi + c\varphi s\theta c\psi) + z_0 \\ 1 \end{bmatrix}, \tag{10}$$

$$\begin{bmatrix} x_D \\ y_D \\ z_D \\ 1 \end{bmatrix} = \begin{bmatrix} -\dfrac{b}{2}(-c\varphi s\psi + s\varphi s\theta c\psi) + x_0 \\ -\dfrac{b}{2}c\theta c\psi + y_0 \\ -\dfrac{b}{2}(s\varphi s\psi + c\varphi s\theta c\psi) + z_0 \\ 1 \end{bmatrix}, \tag{11}$$

The parametric equations in the moving coordinate system can be transformed into the parametric equations $\boldsymbol{W}_M(k_1)$, $\boldsymbol{W}_C(k_2)$ and $\boldsymbol{W}_D(k_3)$ in the absolute coordinate system by the transformation matrix, and the tangent vector at the contact point can accordingly be obtained. The tangent vector at the contact point is perpendicular to the normal vector of the tangent plane, and the normal $\boldsymbol{n}$ vector is $(0, -y_T, z_T)$.

$$\boldsymbol{W}_M(k_1) = [h + r\cos k_1 \quad 0 \quad r\sin k_1], \tag{12}$$

$$\boldsymbol{W}_C(k_2) = [r\cos k_2 \quad \frac{b}{2} \quad r\sin k_2], \tag{13}$$

$$\boldsymbol{W}_D(k_3) = [r\cos k_3 \quad -\frac{b}{2} \quad r\sin k_3], \tag{14}$$

$$\frac{d\boldsymbol{W}_i(k_i)}{dt} \cdot \boldsymbol{n} = 0, \tag{15}$$

Since the contact point is on the cylinder, the equation for a circle around the cylinder is also satisfied:

$$x^2 + y^2 = R^2. \tag{16}$$

Bringing the wheel center coordinates into equations (15) and (16) there are six equations with a total of nine unknowns, where x_0 is independent. After removing the three equations for solving k_1, k_2, and k_3, three equations remain. Therefore, if any two of y_0, z_0, φ, θ and ψ are known, the remaining three variables can be solved for according to the remaining three constraining equations, so that the pose of the robot on the surface can be described.

4 Robot surface stability analysis

When the axis of the rear wheel is in a horizontal position, four positions satisfying the tangent condition can be obtained according to Section 3.2: the top of the cylinder is tangent to the inside and outside of the cylinder, and the bottom of the cylinder is tangent to the inside and outside of the cylinder. Since a wind power blade is an irregular surface of variable curvature, it is still necessary to perform further mechanical analysis of the blade to determine the specific stable operation range of the robot.

4.1 Robot surface sliding analysis

If the friction between the robot and the contact surface is not high enough, the robot may slide as shown in Fig. 8. The center of the blade root section circle is taken as the origin of the global coordinate system, the horizontal direction is taken as the *Y*-axis, the vertical direction is taken as the *X*-axis, and the vertical *XOY* plane direction through the origin is taken as the *Z*-axis. The robot body coordinate system is established with the center of mass of the robot as the origin, the horizontal direction through the origin as the *y*-axis, the vertical direction through the origin as the *x*-axis, and the vertical direction through the origin as the *z*-axis. The angle of rotation of the robot around the *z*-axis in the *XOY* plane is ω_z, the angle of rotation around the y-axis in the *XOZ* plane is ω_y and the angle of rotation around the x-axis in the *YOZ* plane is ω_x.
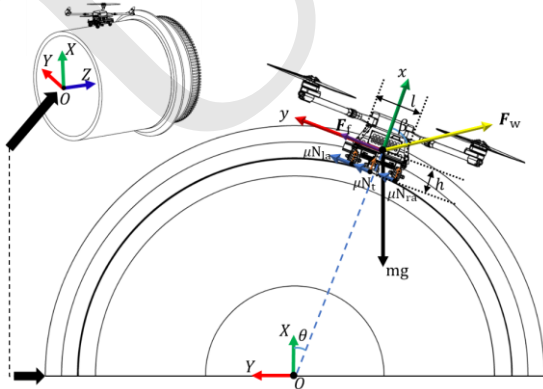
Fig. 8 Force analysis of the robot on a curved surface

When the robot has a certain rotation angle in the

z-axis direction, only gravity acts on the robot body, and the condition under which the robot does not slip on the blade is that the frictional force between the robot and the contact surface is greater than or equal to the sliding component force of the body. Taking the robot at the root of the blade as an example, the stress situation of the robot is analyzed. In order to prevent the robot from slipping, the following conditions should be met:

$$(mg\cos\theta - \boldsymbol{F}_\text{w}\cos\beta)\frac{l}{2} \geq (mg\sin\theta + \boldsymbol{F}_\text{w}\cos\beta - \boldsymbol{F}_\text{f})h,$$

(17)

Where $\boldsymbol{F}_\text{f}$ is:

$$\boldsymbol{F}_\text{f} = \mu\boldsymbol{N}_\text{la} + \mu\boldsymbol{N}_\text{lb} + \mu\boldsymbol{N}_\text{ra} + \mu\boldsymbol{N}_\text{rb} + \mu\boldsymbol{N}_\text{t}, \quad (18)$$

And $\boldsymbol{F}_\text{w}$ is:

$$\boldsymbol{F}_\text{w} = C\rho S V^2 / 2, \quad (19)$$

In the above formula, $\boldsymbol{F}_\text{f}$ is the total frictional force encountered by the robot, μ is the friction coefficient, *m* is the mass of the robot, $\boldsymbol{N}_\text{la}$ is the normal force of the left rear wheel of the robot, $\boldsymbol{N}_\text{ra}$ is the normal force of the right rear wheel of the robot, $\boldsymbol{N}_\text{lb}$ is the normal force of the left front wheel of the robot, $\boldsymbol{N}_\text{rb}$ is the normal force of the right front wheel of the robot, and $\boldsymbol{N}_\text{t}$ is the normal force of the phased array ultrasonic probe on the contact surface. m is the mass of the robot body, $\boldsymbol{F}_\text{w}$ is the wind force received by the robot on the blade, *l* is the distance between the two wheels, *h* is the distance between the robot contact surface and the center of mass, θ is the angle between the robot's center of mass and the global coordinate system circle center and the *x*-axis, and β is the angle between the wind direction and the robot body's coordinate system *x*. The black origin in Fig. 8 is the position of the robot's center of mass. *C* is the air resistance coefficient, ρ is the air density, *S* is the wind-exposed area of the object, and *V* is the relative speed between the object and the wind.

At rest, the forces acting on the robot should satisfy the following equilibrium equation on the *XOY* plane:

$$\boldsymbol{F}_\text{f} + \boldsymbol{G}_{xoy} + \boldsymbol{F}_{wxoy} = 0, \quad (20)$$

Where $\boldsymbol{F}_\text{f}$ is the total frictional force on the ro-

bot, and $\boldsymbol{F}_{wxoy}$ and $\boldsymbol{G}_{xoy}$ are the wind and gravitational forces on the robot in the *XOY* plane, respectively. When the wind force and frictional force reach certain maximum values, the robot would be at its final point before sliding (or be sliding at a constant velocity in accordance with Newton's 2nd Law), and the equation becomes:

$$\{\boldsymbol{F}_{\mathrm{f}}\}_{max} + \boldsymbol{G}_{xoy} + \{\boldsymbol{F}_{wxoy}\}_{max} = 0, \qquad (21)$$

Here $\boldsymbol{F}_{\mathrm{f}}$ can be expressed as:

$$\boldsymbol{F}_{\mathrm{f}} = \mu(mg\cos\theta - \boldsymbol{F}_{\mathrm{w}}\cos\beta), \qquad (22)$$

As the wind force exceeds this maximum value, the robot would slide and accelerate, and the equation becomes:

$$\{\boldsymbol{F}_{\mathrm{f}}\}_{max} + \boldsymbol{G}_{xoy} + \{\boldsymbol{F}_{wxoy}\}_{max} \geq 0, \qquad (23)$$

Through the analysis and research of the forces acting on the robot when it is stationary under various conditions, it can be observed that the conditions that must be satisfied for the robot to maintain stability on the surface are as follows:

$$\mu(mg\cos\theta - \{\boldsymbol{F}_{\mathrm{w}}\}_{max}\cos\beta) \geq mg\sin\theta + \{\boldsymbol{F}_{\mathrm{w}}\}_{max}\sin\beta. \qquad (24)$$

This analysis is carried out under ideal conditions, but of course unideal circumstances may occur in the real world. Therefore, In actual testing, it is important to always consider the impact of changes in angle on the stability of the robot. The maximum deflection angle of the robot can be obtained by Eqs. (19), (22) and (24).

4.2 Robot surface stability range analysis

WTB are complex surfaces designed based on hydrodynamics, making them challenging to describe using simple equations. Currently, aerodynamic design methods for blades primarily apply momentum theory, Bates theory, and blade element theory. Among these, blade element theory is the most widely employed. It involves dividing the blade into several equidistant radial segments, with each micro-segment referred to as a blade element. This approach enables the analysis of the blade in two-dimensional space.

We conduct the following blade element analysis using a 69 m long, 2 MW wind turbine blade. The blade of a wind turbine can be categorized into three main sections based on their positions: the blade root, blade middle, and blade tip. The blade root is typically connected to the wind turbine's nacelle in a standard cylindrical shape, while the blade middle and blade tip exhibit an elliptical form. Initially, the blade was cut along the radial interval of 2000 mm, and the resulting section curve was equally divided into 100 points. As depicted in Fig. 9, the spatial coordinates of the section curve were obtained, and the middle 60 coordinate points were selected for elliptical fitting using the least squares method. These 60 points effectively encompass the coordinate points of the primary beam area on both the windward and leeward sides of the blade.
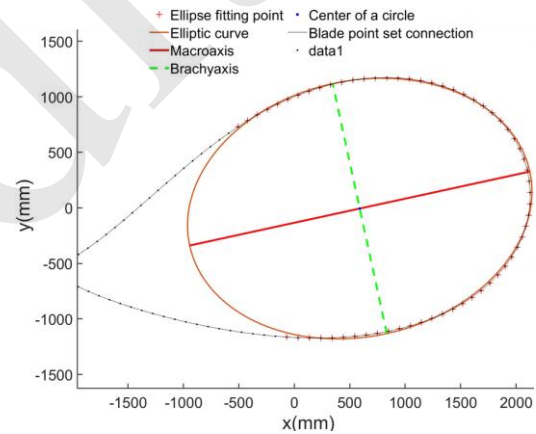
Fig. 9 Elliptical fitting of the wind turbine blade cross-section

The general equation for an ellipse can be expressed as follows:

$$Ax^2 + Bxy + Cy^2 + Dx + Ey + F = 0, \qquad (25)$$

Or expressed as a vector:

$$\boldsymbol{x} \cdot \boldsymbol{a} = 0, \qquad (26)$$

Where $\boldsymbol{a}=[A, B, C, D, E, F]$, $\boldsymbol{x}=[x^2, xy, y^2, x, y, 1]$, N point sets are: (x_i, y_i), $i=1,2,3,\dots N$.

$$D_{\min} = \sum_{i=1}^{N} (\boldsymbol{x} \cdot \boldsymbol{a})^2. \qquad (27)$$

The best-fitting ellipse can be obtained by using the least squares method to minimize the above expression. According to the fitting results, the difference between different sections is mainly the length and torsion angle of the long and short axis of the ellipse, so it can be said that the curvature of the main beam is different depending on the part of the section. The fitting results are shown in Fig. 10.
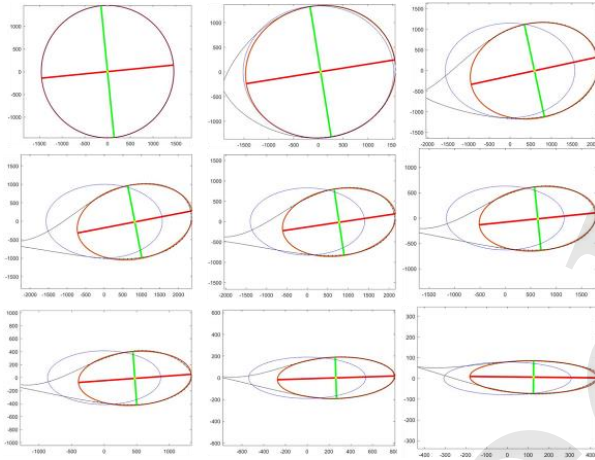
Fig. 10 Section-fitting diagram of the wind turbine blade at different positions (part)

Analyzing the fitting results, most section curves of WTBs can be represented more accurately by using the least squares method to fit ellipses to the plane point sets. Parameters of 32 section curves were obtained through the elliptical fitting, including the semi-major axis a, semi-minor axis b, center coordinates (m, n), and inclination angle γ.

When the robot is positioned on an elliptical cylinder, the derivation of the first two sections remains applicable, but the cylindrical equation is instead replaced by the elliptical cylinder equation. The fitted elliptical equation can be considered as the outcome of translating and rotating the standard elliptical equation. The intersection points between the center of the over ellipse and the first function, with the maximum inclination angle as the slope, represent the theoretical stable range boundary of the robot's center of mass. Additionally, the intersection point between the ellipse and the vertical line of the center of the over ellipse is the center point where the robot's

center of mass remains stable in theory. The system of equations in Eq. (28) describes the points at which the ellipse intersects with the line passing through the center of the fitting ellipse, and the maximum inclination is used as the slope.

$$\begin{cases} \dfrac{((x-m)\cos\gamma + (y-n)\sin\gamma)^2}{a^2} + \\ \dfrac{((m-x)\cos\gamma + (y-n)\sin\gamma)^2}{b^2} = 1 \\ y_{1i} = \tan\theta_{max} x_i + b \\ y_{2i} = -\tan\theta_{max} x_i + b \\ x_i = m \end{cases} \qquad (28)$$

Where (m, n) is the center coordinate of the fitted ellipse in the original blade coordinate system, and γ is the angle of rotation of the ellipse about the center of the circle. y_{1i} and y_{2i} are the first function of the center of the circle with the maximum inclination as the slope, where $i=1,2,3... 32$. $x_i=m$ represents the line that passes through the center of the circle and is parallel to the y-axis. By substituting the parameters of 32 groups of ellipses into Eq. (28), 192 coordinates of intersection points can be obtained. In this study, the windward side of wind turbine blade is taken as the subject, and we use 96 coordinates of intersection points, as shown in Fig. 11.
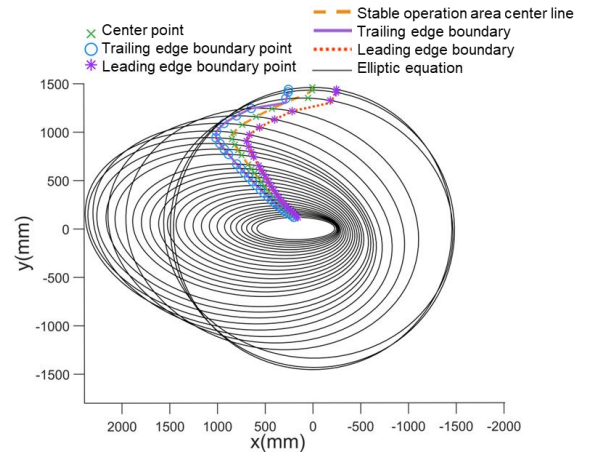
Fig. 11 Robot stable operation area
(Remark: The stable operation area of the robot completely includes the main beam of the blade)

In Fig. 11, the purple solid line on the left and the red dotted line on the right represent the theoretical operational boundaries of the robot's center of mass,

while the area near the middle yellow line segment denotes the theoretical stable operation area of the robot's center of mass. We aim to establish a reference range for the wheeled robot's center of mass to operate on the windward surface of the wind turbine blade. The width of the actual vehicle body, the long axis of the fitted ellipse, and the frictional force between the wheel and the blade impose constraints, causing the feasible range of the robot at different blade positions to constantly change. Therefore, during actual operation, it is essential to continuously adjust the robot's movement path and attitude in real time to ensure stable operation on the blade surface.

5 Simulation and experiment

5.1 Robot motion simulation

In the simulation, the negative direction of the axis corresponds to the movement direction of the robot, with the *x*-axis representing the horizontal direction and the *y*-axis being perpendicular to the *XOZ* plane, opposite to the direction of gravity. Considering the real-world scenario, the friction coefficient between the robot wheel and the blade surface is 0.25.

(1) Simulation of blade leading edge motion

The simulation of the center of mass velocity and angular velocity of the robot on the leading edge of the blade is shown in Fig. 12 and Fig. 13. In the z-direction, there is initial acceleration and then the velocity stabilizes at approximately -0.25 m/s. Throughout the movement, there is a slight variation in the speed along the x-direction, leading to a gradual accumulation of displacement in the *x*-direction, and resulting in a sliding distance of approximately 0.35 m. When the robot travels along the radial direction of the blade, the angular velocity in the *x*-, *y*-, and *z*-directions fluctuates within a range of 1.5 °/s above and below 0 during the first 13 seconds. Subsequently, after 13 seconds, the angular velocity in the *z*-direction gradually increases over time. At 15 seconds, the robot experiences slippage as the accumulated slip distance exceeds the stable operation range.
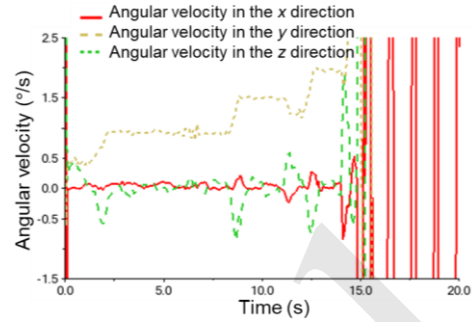

Fig. 12 Simulation of angular velocity motion for the blade leading edge
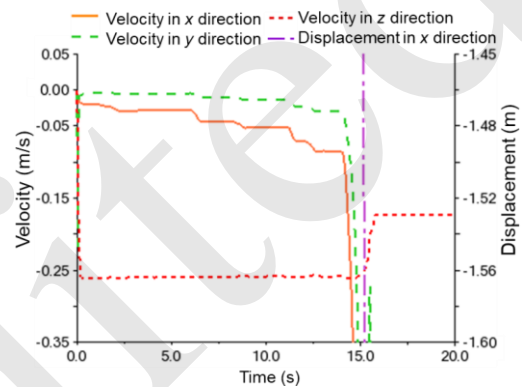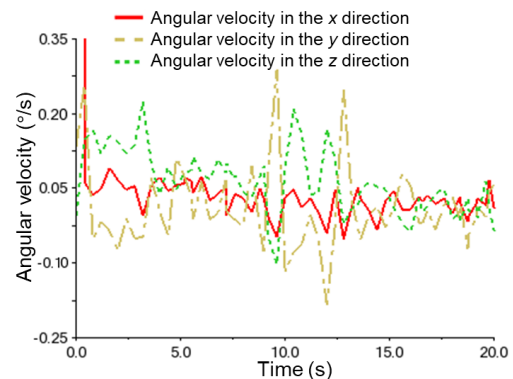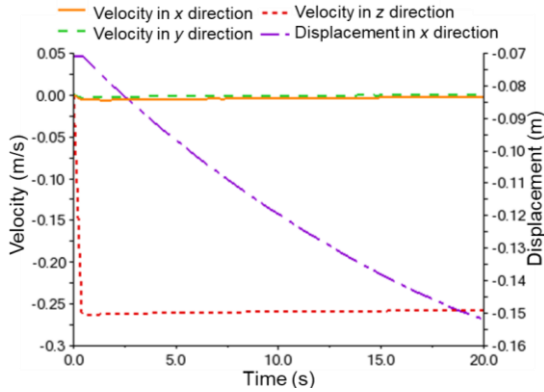

Fig. 13 Velocity and displacement simulation for the blade leading edge

(2) Simulation of mid-blade motion

The motion simulation of the robot in the middle section of the blade is presented in Fig. 14 and Fig. 15. Owing to the minimal curvature change in this region, the robot's velocity in the *x*-, *y*-, and *z*-directions remains relatively stable during the traversal. Over the 20-second duration of the robot's movement, the angular velocity in the *x*- and y-directions fluctuates within a range of 0.35 °/s above and below 0. The slip distance in the *x*-direction measures approximately 0.08 m, and there is an angular change of 2.26 ° in the *z*-direction.

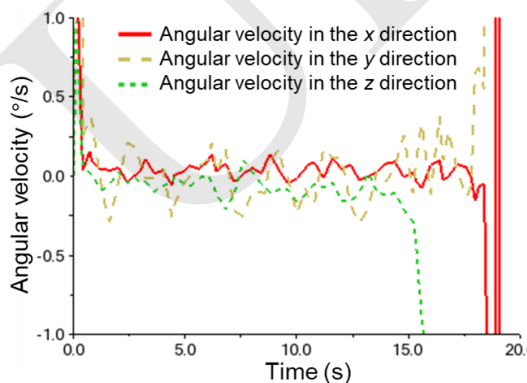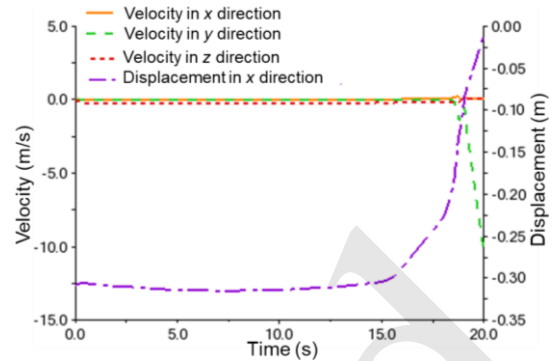**Fig. 15 Velocity and displacement simulation for the mid-blade**

(3) Simulation of blade trailing edge motion

The curvature of the trailing edge of the middle section of the blade exhibits a gentle variation compared to that of the leading edge. The simulation results, depicted in Fig. 16 and Fig. 17, illustrate that as the robot commences its movement, the angular velocity in the *x*-direction initially fluctuates before stabilizing at around 0.37 seconds. Subsequently, from 0.37 seconds to 15 seconds, the angular velocity in the *x*-, *y*-, and *z*-directions fluctuates within a range of about 0.25 °/s above and below 0. Additionally, the *z*-direction angle undergoes a change of approximately 1.8 °. At 15 seconds, the robot experiences slight slippage in the *x*-direction, and at 18 seconds, it slips from the rear edge of the blade due to exceeding the boundary of the stable operating range.

Fig. 16 Simulation of angular velocity motion for the blade trailing edge

Fig. 17 Velocity and displacement simulation for the blade trailing edge

These simulation results demonstrate that the robot can likely traverse the middle section of the blade's front and back edges without any significant slippage. However, when the robot operates at the boundary of the stable operation area of the front and back edges, the sliding distance accumulates as time goes on.

5.2 Robot movement along a curved surface experiment

Due to the long length of the wind power blade, the middle section of a 69 m long, 2 MW blade is utilized as the test subject. This section of the blade measures 3 m in length, 2.3 m in width, and 0.8 m in height. The design parameters of the experimental prototype are outlined in Table 1.

Table 1 Measured data of the experiments in five states

Argument	Value	Argument	Value
Robot weight (kg)	27	Drive wheel radius (mm)	50
Rotor expansion dimensions (mm)	1100*1100	Robot speed (m/s)	0.25
Body width (mm)	370	Probe scan area(mm)	70*130
Body length (mm)	500	Single scan stroke (mm)	200
Body height (mm)	150	Scanning speed (m/s)	0.1

(1) Horizontal position motion

When the robot moves parallel to the radial direction of the blade, with no deflection angle along the axis (as illustrated in Fig. 18), it can traverse from one end of the experimental blade to the other. The

angle of the robot body only changes by 2.43 ° in the *z*-direction from the initial position to the end of the experimental blade, and there is no noticeable sliding along the left- and right-side edges of the blade.
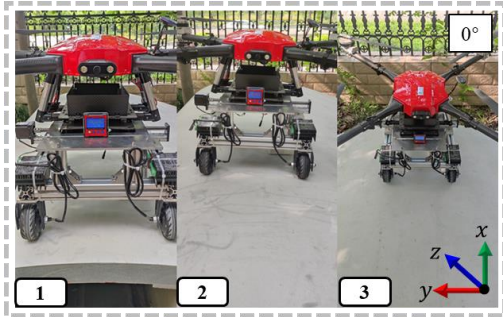

Fig. 18 Wind turbine blade midsection motion test

(2) Robot motion test at the stable range boundary

Within the range of the maximum deflection angle, the deflection angle is randomly selected as -5.24 ° and 9.96 ° at the leading edge and trailing edge of the blade, respectively, the actual testing process as shown in Fig. 19 A and B. The test data is shown in Fig. 20 When the deflection angle is -5.24 °, the robot can move stably from one section of the experimental blade to the other end, and the angle changes to 3.43 ° with respect to the *z*-axis, and slides 0.18 m along the side edge of the blade in the *y*-direction. When the deflection angle is 9.96 °, the robot moves from one part of the experimental blade to the other end, and the posture of the body will change significantly as the operating distance increases. The angle with respect to the *z*-axis in this process changes to 4.05 °, and the deviation distance of the robot along the side edge in the *y*-axis direction (from the initial position to the end position) is about 0.24 m. According to the experimental results, although slippage does occur, the overall operating attitude is relatively stable within the feasible range.
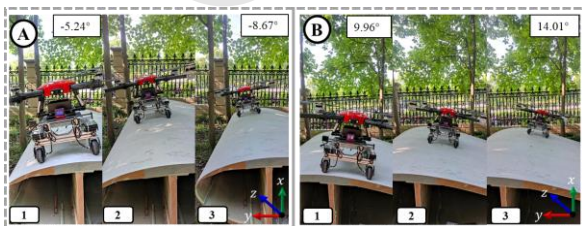

Fig. 19 Experiments on the front and rear edge motion of the robot in the stable running range
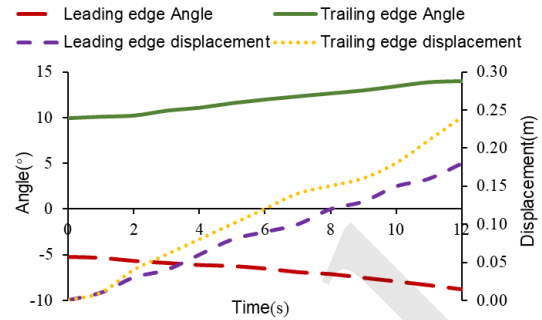

Fig. 20 Robot motion Angle and displacement change

(3) The robot is tested with θ_{max} motion

From the above analysis, it can be determined that the maximum deflection angle of the robot on WTB is 14.06 °. As illustrated in Fig. 21 A and B, the stability of the robot is tested separately at the front and back edges of WTB. The test results of the robot at the stable boundary are presented in Fig. 22. During the initial phase of the stable operating boundary, there is a slight angular deflection and small sliding displacement. However, at approximately 10 seconds, the robot's position shifts outside the stable range boundary due to sliding, and the robot will eventually slide off the top of the blade. Based on the experimental tests, while the robot can function beyond the stable boundary, its primary task involves inspecting the main beam of the wind power blade, which is situated within the stable operational region. Furthermore, for the safety of robot operations, it is advisable for the robot to minimize movements outside the stable operational range.
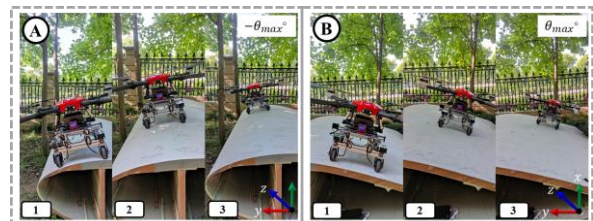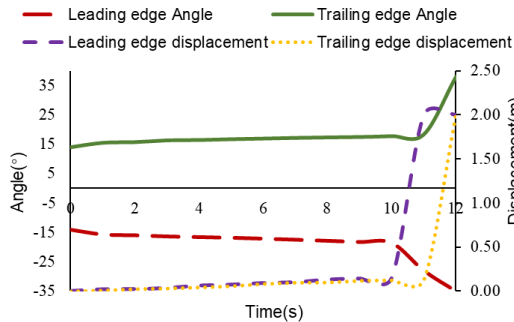

**Fig. 21 The robot is tested with the maximum deflection angle θ_{max}**

Fig. 22 The robot is tested with the maximum deflection angle θ_{max}

(4) Surface adaptive phased array ultrasonic scanning mechanism test

When the robot body is deflected by 0°, 5.24°, and 14.06°, respectively, as shown in A, B, and C of Fig. 23, the ultrasonic probe is still closely attached to the surface of the wind turbine blade. This demonstrates that effective coupling is likely achieved.
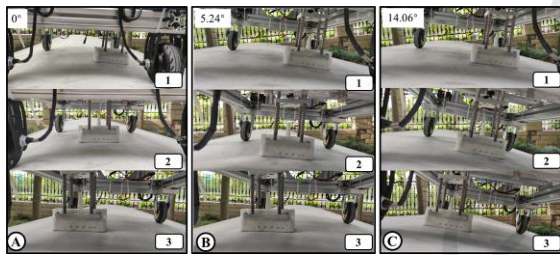
Fig. 23 Adaptive scanning mechanism motion experiment (The 3D printed probe model was utilized for experimental testing in this case.)

(5) Three rounds of posture stability test

As shown in Fig. 24, the stability of the robot under three-wheeled forces (i.e., left front wheel, left rear wheel, right front wheel, and right rear wheel) is tested with the robot has a deflection Angle in all three axes. The experimental results show that the robot can still maintain a stable state under three-wheeled forces.

**Fig. 24 Three rounds of stability tests**

(6) Flight test

The robot's flight capability is evaluated in an actual outdoor environment. Test results indicate that under normal weather conditions, the robot maintains a relatively stable flight attitude under its weight, and successful takeoff and landing are achieved. The experimental process is illustrated in Fig. 25.
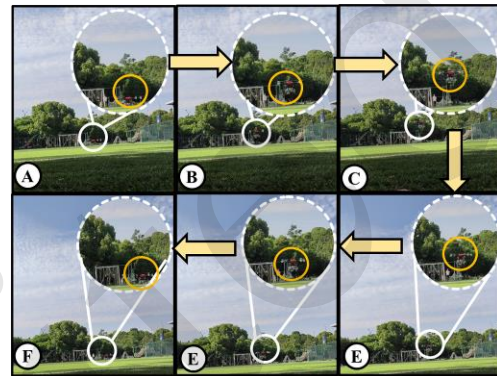
Fig. 25 Robot flight test

(7) Wind resistance test

In this experiment, a 220 V, 2.2 kW axial flow fan with a fan air volume of 18700 m3/h and a maximum wind speed of 15 m/s was used to apply wind resistance to the robot. Wind speed was measured using a hand-held anemometer. The wind resistance performance of the robot was evaluated when the wind speed was 11 m/s. The test results, as shown in Fig. 26, indicate that the robot can maintain a stable posture for an extended period, even under these significant wind speeds.
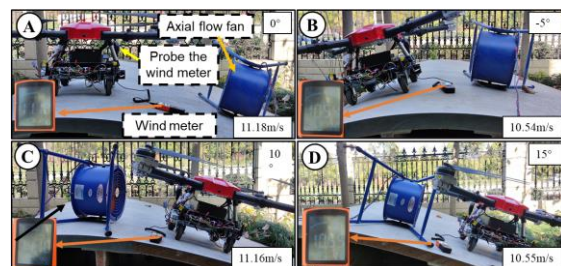
Fig. 26 Wind resistance test

5 Conclusions

We presented a design for a wheel-wing composite robot that can detect potential hazards in the main beam of wind turbine blades (WTBs) during

operation, and validated the design through theoretical analysis and simulation experiments.

To detect potential hazards in the main beam of WTBs during operation, a robot that combines a rotor UAV and wheeled mobile robot was designed. It is equipped with a phased array ultrasonic scanning mechanism that can adapt to blade surfaces with multiple degrees of freedom, and detect potential hazards in main beams with varying curvatures.

We described the pose of the composite robot on a curved surface. Through kinematic calculations and pose analysis, the maximum deflection angle of the robot is determined to be ±14.06°. The blade section is regularized using an ellipse-fitting method, and the stable operation area of the robot on the blade is identified.

Experimental results demonstrated that the robot can maintain stable operation on the blade surface with friction alone, and can detect flaws on the main beam of the experimental blade at a speed of 0.1 m/s.

In summary, we proposed a scheme for detecting flaws on the main beam of WTBs using a wheel-wing composite robot, which can enhance detection efficiency and simplify structural designs. The theoretical analysis of the kinematics of the robot on variable curvature surfaces serves as a reference for studies on the kinematics of wheeled-objects on irregular surfaces, which can be useful in other domains. Regarding engineering design, the composite robot scheme and surface-adaptive structural design can provide valuable insights into future development of wind power blade inspection robots.

However, there are a few aspects which warrant further investigation. First, the utilization of UAVs for delivery lacks long-term operational feasibility, leading to restricted time for executing detection tasks. Second, the robot's reliance on friction for stability, driven by the pursuit of lightweight design, results in a poor ability to withstand external uncertainties. Furthermore, the control system of the robot and the associated software design are not flawless, as evidenced by challenges in defect positioning, vehicle body alignment during detection, and autonomous detection capability.

Moving forward, we reflect upon and propose several solutions for the aforementioned issues. For instance, integrating hybrid drones could enhance the endurance of robot operations. Also, a vacuum ad-

sorption device or a scheme involving the reverse rotation of UAV rotors could bolster the robot's stability. Additionally, the development of a multi-sensor fusion motion control algorithm could enable real-time monitoring of the robot's attitude, enabling autonomous inspection and positioning. Additionally, the robot could be outfitted with diverse testing or maintenance equipment tailored to specific requirements. For instance, maintenance tools could be deployed to repair minor damages, and a protective coating could be applied to the blade surface.

Acknowledgments

Author contributions

As the main person in charge of the project, Jindan WANG was mainly responsible for the hardware construction and software system design of the composite robot, and contributed to the first draft of the paper; Binrui WANG and Xiaolong MA led the overall design of the project, and contributed to the overall framework of the paper; Xin WANG and Lan ZHANG gave guidance on the theoretical analysis and experimental scheme of the robot; Xinghan ZHU contributed to the experimental design and participated in the entire experimental testing process.

Conflict of interest

Jindan WANG, Xin WANG, Lan ZHANG, Xinghan ZHU, Xiaolong MA, and Binrui WANG declare that they have no conflict of interest.

References

Car M, Markovic L, Ivanovic A, et al., 2020. Autonomous Wind-Turbine Blade Inspection Using LiDAR-Equipped Unmanned Aerial Vehicle. *IEEE Access*, 8(8):131380-131387.
https://doi.org/10.1109/access.2020.3009738

Chou JS, Ou YC, Lin KY., 2019. Collapse mechanism and risk management of wind turbine tower in strong wind. *Journal of Wind Engineering and Industrial Aerodynamics*,193(1):0167-6105.
https://doi.org/10.1016/j.jweia.2019.103962

Cieslak C, Shah A, Clark B, et al., 2023. Wind-Turbine Inspection, Maintenance and Repair Robotic System. Volume 14: Wind Energy, p.1-11.
https://doi.org/10.1115/GT2023-101713

Civera M, Surace C, 2022. Non-Destructive Techniques for the Condition and Structural Health Monitoring of Wind Turbines: A Literature Review of the Last 20 Years. *Sensors*, 22(4):1627.
https://doi.org/10.3390/s22041627

Fan JC, Yang CJ, Chen YH, et al., 2018. An underwater robot with self-adaption mechanism for cleaning steel pipes with variable diameters. *Industrial Robot*, 45(2):193-205. https://doi.org/10.1108/IR-09-2017-0168

Franko J, Du S, Kallweit S, et al., 2020. Design of a Multi-Robot System for Wind Turbine Maintenance. *Energies*, 13(10):2552-. https://doi.org/10.3390/en13102552

Gu, WB, Hu DW Cheng L, et al., 2020. Autonomous Wind Turbine Inspection using a Quadrotor. 2020 International Conference on Unmanned Aircraft Systems (ICUAS), p.709-715. https://doi.org/10.1109/ICUAS48674.2020.9214066

Guo ZW, Wang BR, Luo HH et al., 2017. Contact force com pliance control of wall-climbing robot based on passive observation and Control. *Acta Solar Energy Sinica*, 38 (02):503-508 (in Chinese). https://doi.org/CNKI:SUN:TYLX.0.2017-02-031.

Hayashi S, Takei T, Hamamura K, et al., 2017. Moving mech anism for a wind turbine blade inspection and repair ro bot, 2017 IEEE/SICE International Symposium on Sys tem Integration (SII), p.270-275. https://doi.org/10.1109/sii.2017.8279224

Joshua Q, Stephen C, Alexander S, 2016. Kinematic Control of a Mobile Robot Performing Manufacturing Tasks on Non-Planar Surfaces. *Journal of Automation, Mobile Robotics & Intelligent Systems*,10(3):12-21. https://doi.org/10.14313/JAMRIS_3-2016/19

Jung S, Shin JU, Myeong W, et al., 2015. Mechanism and system design of MAV(Micro Aerial Vehicle)-type wall-climbing robot for inspection of wind blades and non-flat surfaces. 15th International Conference on Con trol, Automation and Systems (ICCAS), p.1757-1761. https://doi.org/10.1109/iccas.2015.7364634

Kocer BB, Lachlan O, Brett S, et al., 2022. An Intelligent Aerial Manipulator for Wind Turbine Inspection and Repair. 2022 UKACC 13th International Conference on Control (CONTROL), p.226-227. https://doi.org/10.1109/control55989.2022.9781451

Lee DG, Oh S, Son HI, 2016. Wire-driven parallel robotic system and its control for maintenance of offshore wind turbines. In 2016 IEEE International Conference on Ro botics and Automation (ICRA), p.902-908. https://doi.org/10.1109/ICRA.2016.7487221

Li JC, Cao L, Xiao XH, 2019. Design and adsorption stability analysis of wall climbing robot based on wheeled mag netic adsorption for ultrasonic detection. *Journal of Central South University (Science and Technology)*, 50 (12):2989-2997 (in Chinese). https://doi.org/10.11817/j.issn.1672-7207.2019.12.008

Padrigalan KE, Liu JH, 2023. A Wind-Turbine-Tower-Climb ing Robot Prototype Operating at Various Speeds and Payload Capacity: Development and Validation. *Appl. Sci*, 13(3):1381. https://doi.org/10.3390/app13031381

Sadeghian R, Sareh S, 2021. Multifunctional arm for telero botic wind turbine blade repair. In 2021 IEEE Interna tional Conference on Robotics and Automation (ICRA), p.6883-6889. https://doi.org/10.1109/ICRA48506.2021.9560968

Sahbel A, Abbas A, 2019. System Design and Implementation of Wall Climbing Robot for Wind Turbine Blade Inspec tion. 2019 International Conference on Innovative Trends in Computer Engineering (ITCE), p.242-247. https://doi.org/10.1109/ITCE.2019.8646326

Sahni R, Yoozbashizadeh M, Wahlstrom A, et al., 2022. Ro botic system for wind turbine airfoil maintenance. US Patent 11384739.

Sareh S, Sadeghian R, 2022. Robotic repair system, US Patent 20240018942.

Song ZJ, Ren HL, Zhang JW, et al., 2016. Kinematic Analysis and Motion Control of Wheeled Mobile Robots in Cy lindrical Workspaces. *IEEE Transactions on Automation Science and Engineering*, 13(2):1207-1214. https://doi.org/10.1109/tase.2015.2503283

Wang Y, Zhang XJ, Zhang ML, et al., 2021. Design and Analysis of Split-flexible Wall-climbing Robot with Adaptive Variable Curvature Facade. *Journal of Me chanical Engineering*, 57(3):49-58. https://doi.org/10.3901/jme.2021.03.049

Wang YF, Lu Q, Ren BB., 2023. Wind Turbine Crack In spection Using a Quadrotor With Image Motion Blur Avoided. *IEEE Robotic and Automation Letters*, 8(2): 1069-1076. https://doi.org/10.1109/lra.2023.3236576

Xu C, Liu HD, Zhao ZF, et al., 2022. Design of robot system for oil cleaning and non destructive testing of wind tur bine tower. *Equipment Management and Maintenance*, (14):50-53 (in Chinese). https://doi.org/10.16621/j.cnki.issn1001-0599.2022.07D .22

Zhang Y, Dong L, Chen RH, et al., 2021. Design and Kine matic Analysis of Crawler-type Pipeline Endoscope Ro bots for Wind Turbine Blades. *China Mechanical Engi neering*, 32(15):1884-1889 (in Chinese). https://doi.org/10.3969/j.issn.1004-132X.2021.15.015

中文概要

题　目：风电叶片检测机器人运动建模与稳定性分析

作　者：王金丹 [1]，马小龙 [1]，朱星翰 [1]，王鑫 [2]，张兰 [2]，王斌锐 [1]

机　构：[1] 中国计量大学，机电工程学院，中国杭州，310018；[2] 之江实验室，中国杭州，311121

目　的：目前大多数风电叶片检测机器人体积重量较大，且无法方便的检测叶片主梁隐患。本文旨在设计一种体积小、重量轻、效率高的风电叶片主梁检

测机器人实现对风电叶片主梁隐患的检测。

创新点： 1.提出了轮翼复合机器人的设计方案；2.设计了一种曲面自适应扫查机构；3.实现了叶片截面曲面的规则化处理；4.建立了轮式机器人曲面上位姿描述方法。

方 法： 1.首先建立了机器人整机模型，并针对风电叶片的非规则曲面设计了变曲率曲面自适应检测装置；2.为准确描述叶片表面的弧形特征，采用叶素截面微分和最小二乘拟合椭圆的方法对不规则截面曲线进行数值分析，并建立了机器人在不同截面特征下的位姿描述方程，确定机器人在非结构化环境中的可稳定移动范围；3.然后基于虚拟样机技术，对机器人在叶片上不同位置的运行状态进行了仿真，最后通过样机测试实验验证了机器人设计的合理性。

结 论： 1.风电叶片可采用基于叶素理论微分和椭圆拟合的方法进行规则化处理；2.曲面上轮式机器人位姿描述可由单轮位姿描述推广到多轮位姿描述；3.本文设计的轮翼复合机器人能够仅靠车轮与叶片表面的摩擦力，在与竖直方向呈±14.06°夹角的区域内以 0.25m/s 的速度在实验叶片上方稳定行走和停留，同时可实现以 0.1m/s 的速度对叶片主梁区域自适应耦合扫查。

关键词： 复合机器人；风电叶片；变曲率曲面；稳定性；无损检测